An innovative wheel–rail contact model for railway vehicles under degraded adhesion conditions

DOI 10.1007/s11044-013-9405-4

Multibody System Dynamics manuscript No.
(will be inserted by the editor)

An Innovative Wheel-Rail Contact Model for Railway Vehicles Under Degraded Adhesion Conditions

E. Meli · **A. Ridolfi**

Received: date / Accepted: date

Abstract The accurate modelling of the wheel-rail contact plays a fundamental role in the railway field since the contact forces heavily affect the vehicle dynamics, the wear of the contact surfaces and the vehicle safety. Concerning the wheel-rail contact, an important open problem is represented by the degraded adhesion. A realistic adhesion model is quite difficult to obtain because of the complex and highly nonlinear behaviour of the adhesion coefficient and the presence of external unknown contaminants (the third body); this is especially true when degraded adhesion and large sliding between the wheel and rail contact surfaces occur.
In this work the authors present an adhesion model particularly developed to describe degraded adhesion conditions. The new approach will have to be suitable to be employed within the wheel-rail contact models typical of the multibody applications. In other words the contact model, comprising the new adhesion model, will have to guarantee a good accuracy and, at the same time, a high numerical efficiency to be implemented directly online inside the general multibody model of the vehicles (e.g. in Matlab-Simulink or Simpack environments). [1][2]
The model analysed in the paper is based on some of the main phenomena characterising the degraded adhesion, such as large sliding at the contact interface, high energy dissipation, the consequent cleaning effect on the contact surfaces and the final adhesion recovery due to the removal of external unknown contaminants.
The adhesion model has been validated thanks to the experimental data provided by Trenitalia S. p. A. coming from on-track tests performed in Velim (Czech Republic).

E. Meli · A. Ridolfi
Department of Industrial Engineering, University of Florence, Via S. Marta n. 3, 50139 Florence, Italy
Tel.: +39-0554796332
Fax: +39-0554796342

E. Meli - E-mail: enrico.meli@unifi.it

A. Ridolfi - E-mail: a.ridolfi@unifi.it

The tests have been carried out on a straight railway track under degraded adhesion conditions with the railway vehicle UIC-Z1 equipped with a fully-working Wheel Slide Protection (WSP) system.
The validation highlighted the good performances of the adhesion model in terms of accuracy and numerical efficiency. In conclusion, the adhesion model turned out to be able to well reproduce the complex phenomena behind the degraded adhesion.

Keywords Multibody modelling of railway vehicles · Wheel-rail contact · Degraded adhesion · Adhesion recovery.

1 Introduction

The accurate modelling of the wheel-rail contact plays a fundamental role in the railway field since the contact forces heavily affect the vehicle dynamics, the wear of the contact surfaces and the vehicle safety.
In the multibody applications the numerical performances (computation times and memory consumption) are very important; therefore, in practice, it is usually impossible to model the contact by considering the wheel and the rail as generic elastic continuous bodies. Generally the multibody contact models are characterized by three main logical parts: the contact point detection, the normal problem solution and the tangential problem solution, that includes the adhesion model.
The contact point detection allows the calculation of the contact point position on the wheel and rail surfaces. The most important approaches make use either of constraint equations [39][38] or of exact analytical methods aimed at the reduction of the algebraic problem dimension. [13][31][9][20] The solution of the normal problem is generally based on the Lagrange multipliers [39][38] and on improvements of Hertz theory.[6][10][26] Concerning the solution of the tangential problem, different approaches have been taken into account in the last decades. The most significant strategies comprise the linear Kalker theory saturated according to Johnson-Vermeulen formula [26][27][17][25][19], the non-linear Kalker theory implemented in the FASTSIM algorithm [26][27][24][23][29][22] and Polach theory [35][34][36][37] that permits to describe the decrease of the adhesion coefficient with increasing creepage (excluding the contact spin) and to better fit the experimental data. All the three steps of the contact model have to guarantee a good accuracy and a high numerical efficiency to implement the contact model direclty online inside more general multibody vehicle models (developed in dedicated environments like Matlab-Simulink and Simpack), without employing discretized look-up table (LUT). [1][2]
The main approaches followed to solve the tangential problem (including the adhesion model) usually do not consider the important issue of the degraded adhesion between wheel and rail, that remains still an open problem. The substantial lack of literature concerning these topics is mainly caused by the difficulty to obtain a realistic adhesion law because of the complex and non-linear behaviour of the adhesion coefficient and the presence of external unknown contaminants (the third body). This is especially true when the degraded adhesion yields a high energy dissipation and, consequently, an adhesion recovery.

Over the years, many important studies and analyses have been perfomed to investigate the role of so-called third body between the contact surfaces. In particular the analyses have been carried out both on laboratory test rigs and through on-track railway tests by taking into account natural and artificial external contaminants and friction modifiers. [7][8][45][32][21][18][16][14]
At the same time, to better understand the non-linear behaviour characterising the degraded adhesion, also the high energy dissipation at the contact interface and the consequent adhesion recovery have begun to be more accurately studied. [12] [46] [11] [44] [15] [5] [4][30]
The adhesion model presented by the authors in this work aims to improve the description accuracy of degraded adhesion conditions in multibody vehicle dynamics and railway systems. According to the recent trends of the state of the art (see the previous bibliographic references), the new model focuses on the main phenomena characterising the degraded adhesion, paying particular attention to the energy dissipation at the contact interface, the consequent cleaning effect and the resulting adhesion recovery due to the removal of external unknown contaminants. Besides, since most of the physical characteristics of the contaminants are totally unknown in practice, the followed approach will have to minimize the number of hardly measurable physical quantities required by the model.
The new model will have to guarantee a good accuracy to well reproduce the non-linear phenomena behind the degraded adhesion; contemporaneously it will have to ensure high computational performances so that the whole contact model (comprising the adhesion model) could be directly implemented online inside more general multibody vehicle models.
The adhesion model described in the paper has been thought to be implemented and used in all the main interesting scenarios in the railway field: with different wheel and rail profiles, with generic railway tracks (straight or curving) and with multiple contact points. In this preliminary research phase, considering the availability of experimental data, the analysis of the performances of the model is focused on braking manoeuvres performed on straight tracks (which is a crucial case in the study of degraded adhesion).
The adhesion model has been validated thanks to experimental data provided by Trenitalia S. p. A. coming from on-track tests performed in Velim (Czech Republic) with the railway vehicle UIC-Z1. The tests have been carried out on a straight railway track under degraded adhesion conditions with a vehicle equipped with a Wheel Slide Protection (WSP) system.
In chapter 2 the general architecture of the model will be illustrated while in chapter 3 the multibody model, comprising the railway vehicle model and the wheel-rail contact model, will be described in detail. In chapter 4 the experimental data will be introduced and in chapter 5, 6 and 7 the validation of the new model will be discussed. Finally conclusions and further developments will be proposed in chapter 8.

2 General Architecture of the Model

The architecture of the multibody model is briefly reported in Fig. 1.
From a logical point of view, the multibody model consists of two different parts

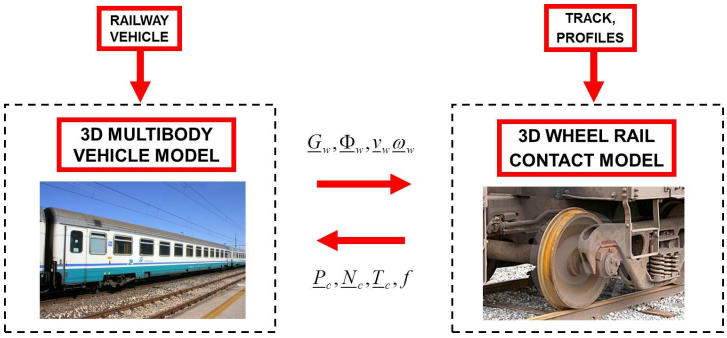

Fig. 1 Architecture of the multibody model.

that mutually interact, directly online, during the dynamical simulation (at each integration time step): the three-dimensional (3D) model of the railway vehicle (the geometrical and physical characteristics of which are known) and the 3D wheel-rail contact model. At each time step the multibody vehicle model calculates the kinematic variables of each wheel (position $\underline{G}_w$, orientation $\underline{\Phi}_w$, velocity $\underline{v}_w$ and angular velocity $\underline{\omega}_w$) while the contact model, starting from the knowledge of these quantities, of the track geometry and of the wheel and rail profiles, evaluates the normal and tangential contact forces $\underline{N}_c$, $\underline{T}_c$ (applied to the wheel in the contact point $\underline{P}_c$) and the adhesion coefficient f, needed to carry on the dynamical simulation. Both the vehicle model and the contact model have been implemented in the Matlab-Simulink environment.
The wheel-rail contact model comprises three different steps (see Fig. 2). The detection of the contact points $\underline{P}_c$ is based on some innovative procedures recently developed by the authors in previous works [31][9][20]. The normal contact problem is then solved through the global Hertz theory [6][10][26] to evaluate the normal contact forces $\underline{N}_c$. Finally the solution of the tangential contact problem is performed by means of the global Kalker-Polach theory [35][34][36][37] to compute the tangential contact forces $\underline{T}_c$ and the adhesion coefficient f.
The strategy to solve the tangential contact problem includes the innovative degraded adhesion model developed by the authors in this work (see Fig. 3). The main inputs of the degraded adhesion model are the wheel velocity $\underline{v}_w$, the wheel angular velocity $\underline{\omega}_w$, the normal force at the contact interface $\underline{N}_c$ and the position of the contact points $\underline{P}_c$. The model also requires the knowledge of some wheel-rail and contact parameters that will be introduced along the paper. The outputs of the degraded adhesion model are the desired values of the adhesion coefficient f and of the tangential contact force $\underline{T}_c$.

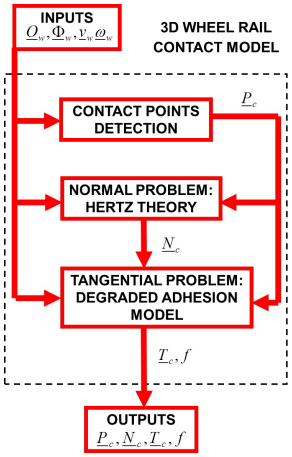

Fig. 2 Architecture of the wheel-rail contact model.

Fig. 3 Inputs and outputs of the degraded adhesion model.

3 The Multibody Model

In this chapter the multibody model is described in detail. Firstly the 3D railway vehicle model will be analyzed; secondly the attention will focus on the 3D wheel-rail contact model (comprising the contact point detection, the normal problem and the tangential problem) and, in particular, on the new degraded adhesion model.

3.1 The Vehicle Model

The considered railway vehicle is the UIC-Z1 wagon (illustrated in Fig. 4 and 5); its geometrical and physical characteristics are provided by Trenitalia S.p.A. [41]. The considered vehicle is equipped with a Wheel Slide Protection (WSP) system.[41][43][5]
The wagon is composed of one carbody, two bogie frames, eight axleboxes and four wheelsets. The primary suspension connects the bogie frame to the four axleboxes and includes flexicoil springs (constituted by two coaxial helical compression springs), vertical hydraulic dampers and axlebox bushings. The longitudinal primary stiffness value may seem quite low (see Tab. 3). This is due to the fact that in the primary suspension stage the traction is transmitted through the links connecting the axleboxes to the bogie frame and the corresponding very stiff axlebox bushings.
The secondary suspension, usually softer than the primary one for comfort reasons, connects the carbody to the bogie frames (see Fig. 6 and 7) and includes pneumatic air springs, dampers (vertical, lateral and longitudinal anti-yaw dampers), lateral

Fig. 4 The UIC-Z1 wagon.

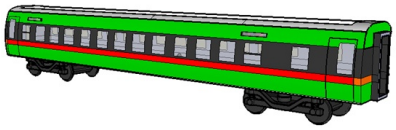

Fig. 5 Multibody vehicle model.

bump-stops, anti-roll bar and traction rod. Lateral bumbstops and anti-roll bar are fundamental to limit the carbody soupless and to avoid loading gauge problems while the traction rod is needed to transmit the traction. In Tab. 1 the main properties of the railway vehicle are given.

The multibody vehicle model takes into account all the degrees of freedom (DOFs)

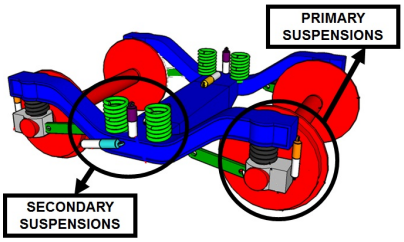

Fig. 6 Primary and secundary suspensions.

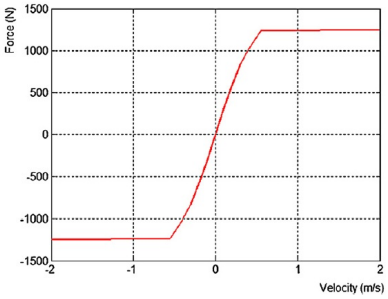

Fig. 7 Example of non-linear characteristic: vertical damper of the primary suspension.

Table 1 Main characteristics of the railway vehicle

Parameter	Units	Value
Total mass	[kg]	≈ 43000
Wheel arrangement	–	2-2
Bogie wheelbase	[m]	2.56
Bogie distance	[m]	19
Wheel diameter	[m]	0.89
Primary suspended masses own frequency	[Hz]	≈ 4.5
Secondary suspended masses (carbody) own frequency	[Hz]	≈ 0.8

of the system bodies (one carbody, two bogie frames, eight axleboxes, and four wheelsets). Considering the kinematic constraints that link the axleboxes and the wheelsets (cylindrical 1DOF joints) and without including the wheel-rail contacts,

the whole system has 50 DOFs. The main inertial properties of the bodies are summarized in Tab. 2.[41]

Both the primary suspension (springs, dampers and axlebox bushings) and the sec-

Table 2 Inertial properties of the rigid bodies

Body	Mass [kg]	I_{xx} [kgm^2]	I_{yy} [kgm^2]	I_{zz} [kgm^2]
Carbody	≈ 29000	76400	1494400	1467160
Bogie	≈ 3000	2400	1900	4000
Wheelset	≈ 1300	800	160	800
Axlebox	≈ 200	3	12	12

ondary suspension (springs, dampers, lateral bump-stops, anti-roll bar and traction rod) have been modelled through 3D visco-elastic force elements able to describe all the main non-linearities of the system (see Fig. 6 and 7). In Tab. 3 the characteristics of the main linear elastic force elements of both the suspension stages are reported.[41] The non-linear elastic force elements have been modelled through non-linear functions that correlate the displacements and the relative velocities of the force elements connection points to the elastic and damping forces exchanged by the bodies. By way of example the non-linear characteristic of a vertical damper of the primary suspension is illustrated in Fig. 7.

Finally, also the Wheel Slide Protection (WSP) system of the railway wagon UIC-

Table 3 Main linear elastic characteristics of the two stage suspensions

Element	Transl. Stiff. x [N/m]	Transl. Stiff. y [N/m]	Transl. Stiff. z [N/m]	Rotat. Stiff. x [Nm/rad]	Rotat. Stiff. y [Nm/rad]	Rotat. Stiff. z [Nm/rad]
Springs of the primary suspension	844000	844000	790000	10700	10700	0
Springs of the secondary suspension	124000	124000	340000	0	0	0
Axlebox bushing	$4 \cdot 10^7$	$6.5 \cdot 10^6$	$4 \cdot 10^7$	45000	9700	45000
Anti-roll bar	0	0	0	$2.5 \cdot 10^6$	0	0

Z1 has been modelled to better investigate the vehicle behaviour during the braking phase under degreded adhesion conditions. [43] [5] The whole vehicle model has been implemented in the Matlab-Simulink environment. [1]

3.2 The Wheel-Rail Contact Model

In this section the three logical parts of the wheel-rail contact model (contact point detection, normal problem and tangential problem) will be analyzed with particular regard to the new degraded adhesion model. The model inputs are the kinematic variables of each wheel (position $\underline{G}_w$, orientation $\underline{\Phi}_w$, velocity $\underline{v}_w$ and angular velocity

$\underline{\omega}_w$) together with the track geometry and the wheel and rail profiles while the outputs the normal and tangential contact forces $\underline{N}_c$, $\underline{T}_c$ (applied to the wheel in the contact point $\underline{P}_c$) and the adhesion coefficient f.

3.2.1 The Contact Point Detection

Referring to Fig. 2 the contact point detection algorithm allows the calculation of the contact points $\underline{P}_c$ starting from the wheel position $\underline{G}_w$ and orientation $\underline{\Phi}_w$, the track geometry and the wheel and rail profiles. The detection procedure has been developed by the authors in previous works [31][9][20] and is based on the reduction of the algebraic problem dimension through exact analytical techniques; this reduction represents the main feature of the new algorithm. The main characteristics of the innovative procedure can be summarized as follows:

- it is a fully 3D algorithm that takes into account all the six relative DOFs between wheel and rail;
- it is able to support generic railway tracks and generic wheel and rail profiles;
- it assures a general and accurate treatment of the multiple contact without introducing simplifying assumptions on the problem geometry and kinematics and limits on the number of contact points detected;
- it assures high numerical efficiency making possible the online implementation within the commercial multibody software (like Simpack Rail and Adams Rail) without discrete LUT. [1][2]

The contact point position can be evaluated imposing the following parallelism conditions [13]:

$$\begin{aligned} \underline{n}_r^r(\underline{P}_r^r) \times \underline{n}_w^r(\underline{P}_w^r) = \underline{n}_r^r(\underline{P}_r^r) \times R_w^r \underline{n}_w^w(\underline{P}_w^w) = \underline{0} \\ \underline{n}_r^r(\underline{P}_r^r) \times \underline{d}^r = \underline{0} \end{aligned} \tag{1}$$

where $\underline{P}_w^w(x_w, y_w) = \left(x_w \; y_w \; -\sqrt{w(y_w)^2 - x_w^2} \right)^T$ and $\underline{P}_r^r(x_r, y_r) = \left(x_r \; y_r \; r(y_r) \right)^T$ are the positions of the generic points on the wheel surface and on the rail surface (expressed in the reference systems $G_w x_w y_w z_w$ and $O_r x_r y_r z_r$), $w(y_w)$ and $r(y_r)$ are the wheel and rail profiles (supposed to be known), $\underline{n}_w^w$ and $\underline{n}_r^r$ are the outgoing normal unit vectors to the wheel and rail surfaces (in the reference systems $G_w x_w y_w z_w$ and $O_r x_r y_r z_r$), R_w^r is the rotation matrix that links the reference system $G_w x_w y_w z_w$ to the reference system $O_r x_r y_r z_r$ and $\underline{d}^r$ is the distance vector between two generic points on the wheel surface and on the rail surface (both referred to the reference system $O_r x_r y_r z_r$): $\underline{d}^r(x_w, y_w, x_r, y_r) = \underline{P}_w^r(x_w, y_w) - \underline{P}_r^r(x_r, y_r)$ in which $\underline{P}_w^r = \underline{O}_w^r + R_w^r \underline{P}_w^w(x_w, y_w)$ is the position of the generic point of the wheel surface expressed in the reference system $O_r x_r y_r z_r$ (see Fig. 8).

The first condition of the system (1) imposes the parallelism between the normal unit vectors, while the second one requires the parallelism between the normal unit vector to the rail surface and the distance vector. The system (1) consists of six non-linear equations in the unknowns (x_w, y_w, x_r, y_r) (only four equations are independent and therefore the problem is 4D). However it is possible to exactly express three of the

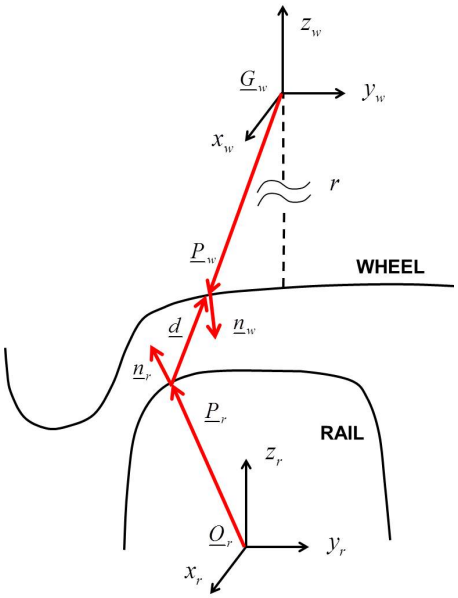

Fig. 8 Wheel-rail contact point detection.

four variables (in this case (x_w, x_r, y_r)) as a function of y_w, reducing the original 4D problem to a single 1D scalar equation in the variable y_w [31][9][20]:

$$F(y_w) = 0. \tag{2}$$

At this point the simple scalar Eq. (2) can be easily solved through appropriate numerical algorithms. Finally, once obtained the generic solution y_{wc} of Eq. (2), the complete solution (x_{wc}, y_{wc}, x_{rc}, y_{rc}) of the system (1) and consequently the contact points $\underline{P}^r_{wc} = \underline{P}^r_w(x_{wc}, y_{wc})$ and $\underline{P}^r_{rc} = \underline{P}^r_r(x_{rc}, y_{rc})$ can be found by substitution.

3.2.2 The Normal Contact Problem

Starting from the kinematic variables of the wheel and the contact point position $\underline{P}_c$, the normal forces $\underline{N}_c$ are calculated through the global Hertz theory for each contact point (see the Fig. 2, 8, 9 and 10): [6][10][26][9]

$$\underline{N}_c = N_c \underline{n}_w \qquad N_c = \|\underline{N}_c\|. \tag{3}$$

The scalar value N_c of $\underline{N}_c$ can be evaluated as follows:

$$N_c = \left[-k_h |p_n|^\gamma + k_v |v_n| \frac{sign(v_n) - 1}{2} \right] \frac{sign(p_n) - 1}{2} \tag{4}$$

where $p_n = max(\underline{d}^r \cdot \underline{n}^r_w, 0)$ is the normal penetration, γ is the Hertz's exponent equal to $3/2$, k_v is the contact damping constant, $v_n = \underline{V}_c \cdot \underline{n}^r_r$ is the normal penetration velocity ($\underline{V} = \underline{v}_w + \underline{\omega}_w \times (\underline{P}_c - \underline{G}_w)$ is the velocity of the contact point rigidly connected

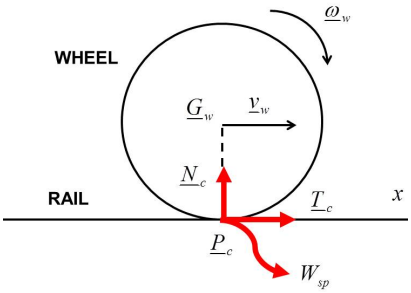

Fig. 9 Contact forces.

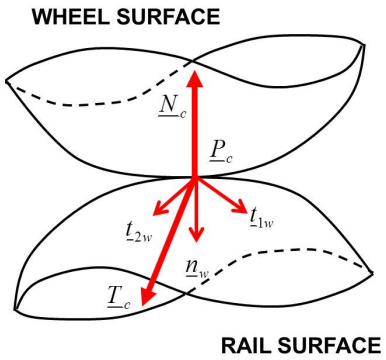

Fig. 10 Contact surfaces.

to the wheel). The quantity k_h is the hertzian constant, function both of the material properties (the Young modulus E, the shear modulus G and the Poisson coefficient σ) and of the contact bodies geometry through the curvatures of the contact surfaces (easily computable if the contact point position $\underline{P}_c$ is known).
Finally it is worth noting that the Hertz theory allows also the calculation of the semi-axes a and b of the elliptical contact patch, depending on the material properties, the curvatures of the contact surfaces and the normal contact force N_c (or, equivalently, the normal penetration p_n). [6][10][26][9]

3.2.3 The Tangential Contact Problem and the Degraded Adhesion Model

In this section the tangential contact forces $\underline{T}_c$ and the adhesion coefficient f will be calculated solving the tangential contact problem [35][34][36][37] Particularly the attention will focus on the new adhesion model especially developed for degraded adhesion conditions. The inputs of the model are kinematic variables of the wheel (position $\underline{G}_w$, orientation $\underline{\Phi}_w$, velocity $\underline{v}_w$ and angular velocity $\underline{\omega}_w$), the contact point position $\underline{P}_c$ and the normal contact forces $\underline{N}_c$ (see the Fig. 2, 3, 8, 9 and 10).
With regard to Fig. 9 and 10, for each contact point $\underline{P}_c$, it is possible to determine the sliding $\underline{s}$ (with its longitudinal and lateral components s_x, s_y):

$$\begin{gathered} \underline{s} = \underline{v}_w + \underline{\omega}_w \times (\underline{P}_c - \underline{G}_w) \\ s = \|\underline{s}\| \qquad s_x = \underline{s} \cdot \underline{t}_{1w} \qquad s_y = \underline{s} \cdot \underline{t}_{2w} \end{gathered} \tag{5}$$

where $\underline{n}_w$, $\underline{t}_{1w}$ and $\underline{t}_{1w}$ are respectively the normal unit vector and the tangential unit vectors (in longitudinal and lateral direction) corresponding to the generic contact point $\underline{P}_c$ (see Fig. 10). Subsequently the creepage $\underline{e}$ can be introduced

$$\begin{gathered} \underline{e} = \frac{\underline{s}}{v_w} \qquad v_w = \|\underline{v}_w\| \\ e_x = \underline{e} \cdot \underline{t}_{1w} \qquad e_y = \underline{e} \cdot \underline{t}_{2w} \end{gathered} \tag{6}$$

together with the adhesion coefficient f and the specific dissipated energy W_{sp} at the contact area:

$$\begin{array}{ccc} T_c = \|\underline{T}_c\| & e = \|\underline{e}\| & f = \frac{T_c}{N_c} \\ T_x = \underline{T}_c \cdot \underline{t}_{1w} = T_c \frac{e_x}{e} & T_y = \underline{T}_c \cdot \underline{t}_{2w} = T_c \frac{e_y}{e} & W_{sp} = \underline{T}_c \cdot \underline{e} = T_c e = f N_c e \end{array} \tag{7}$$

in this way the specific dissipated energy W_{sp} can also be interpreted as the energy dissipated at the contact for unit of distance travelled by the railway vehicle (see Eq. (6) and (7)).

The main phenomena characterising the degraded adhesion are the large sliding occurring at the contact interface and, consequently, the high energy dissipation. Such a dissipation causes a cleaning effect on the contact surfaces and finally an adhesion recovery due to the removal of external contaminants. When the specific dissipated energy W_{sp} is low the cleaning effect is almost absent, the contaminant level h does not change and the adhesion coefficient f is equal to its original value in degraded adhesion conditions f_d. As the energy W_{sp} increases, the cleaning effect increases too, the contaminant level h becomes thinner and the adhesion coefficient f raises. In the end, for large values of W_{sp}, all the contaminant is removed (h is null) and the adhesion coefficient f reaches its maximum value f_r; the adhesion recovery due to the removal of external contaminants is now completed. At the same time if the energy dissipation begins to decrease, due for example to a lower sliding, the reverse process occurs (see Fig. 11 and 12).

Since the contaminant level h and its characteristics are usually totally unknown, it is

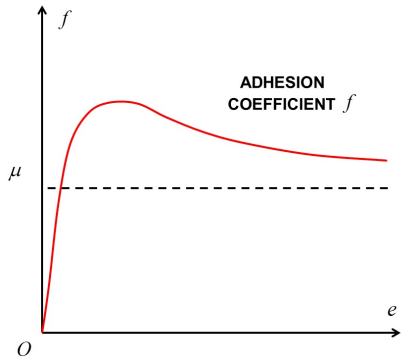

Fig. 11 Standard behaviour of the adhesion coefficient f.

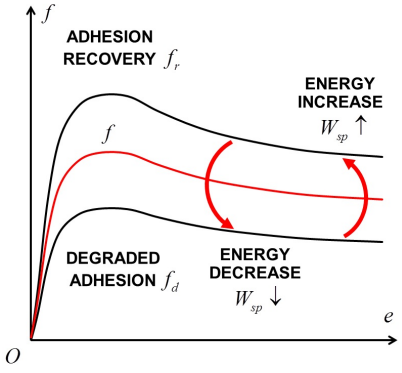

Fig. 12 The adhesion coefficient f and the specific dissipated energy W_{sp} under degraded adhesion conditions.

usefull trying to experimentally correlate the adhesion coefficient f directly with the specific dissipated energy W_{sp} (see Eq. (7)). To reproduce the qualitative trend previously described and to allow the adhesion coefficient to vary between the extreme values f_d and f_r, the following expression for f is proposed:

$$f = [1 - \lambda(W_{sp})] f_d + \lambda(W_{sp}) f_r \tag{8}$$

where $\lambda(W_{sp})$ is an unknown transition function between degraded adhesion and adhesion recovery. The function $\lambda(W_{sp})$ has to be positive and monotonous increasing; moreover the following boundary conditions are supposed to be verified: $\lambda(0) = 0$ and $\lambda(+\infty) = 1$.
In this way the authors suppose that the transition between degraded adhesion and adhesion recovery only depends on W_{sp}. This hypothesis is obviously only an approximation but, as it will be clearer in the next chapters, it well describes the adhesion behaviour. Initially, to catch the physical essence of the problem without introducing a large number of unmanageable and unmeasurable parameters, the authors have chosen the following simple expression for $\lambda(W_{sp})$:

$$\lambda(W_{sp}) = 1 - e^{-\tau W_{sp}} \tag{9}$$

where τ is now the only unknown parameter to be tuned on the base of the experimental data.
In this reseach activity the two main adhesion coefficients f_d and f_r (degraded adhesion and adhesion recovery) have been calculated according to Polach: [35][34][26]

$$\begin{aligned} f_d &= \frac{2\mu_d}{\pi}\left[\frac{k_{ad}\varepsilon_d}{1+(k_{ad}\varepsilon_d)^2} + arctg(k_{sd}\varepsilon_d)\right] \\ f_r &= \frac{2\mu_r}{\pi}\left[\frac{k_{ar}\varepsilon_r}{1+(k_{ar}\varepsilon_r)^2} + arctg(k_{sr}\varepsilon_r)\right] \end{aligned} \tag{10}$$

where

$$\varepsilon_d = \frac{2}{3}\frac{C\pi a^2 b}{\mu_d N_c}e \qquad \varepsilon_r = \frac{2}{3}\frac{C\pi a^2 b}{\mu_r N_c}e. \tag{11}$$

The quantities k_{ad}, k_{sd} and k_{ar}, k_{sr} are the Polach reduction factors (for degraded adhesion and adhesion recovery respectively) and μ_d, μ_r are the friction coefficient defined as follows

$$\begin{aligned} \mu_d &= \left(\frac{\mu_{cd}}{A_d} - \mu_{cd}\right)e^{-\gamma_d s} + \mu_{cd} \\ \mu_r &= \left(\frac{\mu_{cr}}{A_r} - \mu_{cr}\right)e^{-\gamma_r s} + \mu_{cr} \end{aligned} \tag{12}$$

in which μ_{cd}, μ_{cr} are the kinetic friction coefficients, A_d, A_r are the ratios between the kinetic friction coefficients and the static ones and γ_d, γ_d are the friction decrease rates. The Polach approach (see Eq. (10)) has been followed since it permits to describe the decrease of the adhesion coefficient with increasing creepage and to better fit the experimental data (see Fig. 11 and 11).
Finally it has to be noticed that the semi-axes a and b of the contact patch (see Eq. (11)) depend only on the material properties, the contact point position P_c on wheel and rail (through the curvatures of the contact surfaces in the contact point) and the normal force N_c, while the contact shear stiffness C ($\mathrm{N/m^3}$) is a function only of material properties, the contact patch semi-axes a and b and the creepages. More particularly, the following relation holds: [26]

$$C = \frac{3G}{8a}\sqrt{\left(c_{11}\frac{e_x}{e}\right)^2 + \left(c_{22}\frac{e_y}{e}\right)^2} \tag{13}$$

where $c_{11} = c_{11}(\sigma, a/b)$ and $c_{22} = c_{22}(\sigma, a/b)$ are the Kalker coefficients.
In the end, the desired values of the adhesion coefficient f and of the tangential contact force $T_c = fN_c$ can be evaluated by solving the algebraic Eq. (8) in which the explicit expression of W_{sp} has been inserted (see Eq. (7)):

$$f = \Im(f,t) \tag{14}$$

where $\Im$ indicates the generic functional dependence. Due to the simplicity of the transition function $\lambda(W_{sp})$, the solution can be easily obtaind through standard non-linear solvers. [28] From a computational point of view, the adhesion coefficient f_i can be computed at each integration time t_i as follows

$$f_i = \Im(f_i, t_i). \tag{15}$$

Eventually, the vector tangential contact force $\underline{T}_c$ has to be calculated. To this aim the creepage $\underline{e}$ can be employed:

$$\begin{aligned} T_x &= T_c \frac{e_x}{e} \;\; T_y = T_c \frac{e_y}{e} \\ \underline{T}_c &= T_x \underline{t}_{w1} + T_y \underline{t}_{w2}. \end{aligned} \tag{16}$$

In this phase of the research activity concerning the degraded adhesion, the contact spin at the wheel-rail interface has not been considered. The components of the spin moment $\underline{M}_{sp} = M_{sp}\underline{n}_w$ produced by the spin creepage $e_{sp} = \underline{\omega}_w \cdot \underline{n}_w / v_w$ and by the lateral creepage e_y can be neglected because they are quite small. On the other hand the effect of the spin creepage e_{sp} on the lateral contact force T_y may be not negligible. This limitation can be partially overcome thanks to the Polach theory [35][34] that takes into account, in an approximated way, the effect of the spin creepage on the lateral contact force T_{sp}:

$$\begin{aligned} T_x &= T_c^{'} \frac{e_x}{e_m} \\ T_y &= T_c^{'} \frac{e_y}{e_m} + T_{sp} \frac{e_{sp}}{e_m} \end{aligned} \tag{17}$$

where e_m is the modulus of the modified translational creepage $\underline{e}_m$, T_{sp} is the lateral contact force caused by the spin creepage e_{sp} and $T_c^{'}$ is the modulus of the old tangential contact force calculated before. The quantities T_{sp} and $\underline{e}_m$ are evaluated in [34] starting from the geometrical and physical characteristics of the system; however T_{sp}, differently from $T_c^{'}$, does not consider the decrease of the adhesion coefficient with increasing creepage and the adhesion recovery under degraded adhesion conditions introduced by the authors.
More in general, the role of the contact spin under degraded adhesion conditions, especially in presence of adhesion recovery, is still an open problem.

4 The Experimental Data

The degraded adhesion model has been validated by means of experimental data [42], provided by Trenitalia S. p. A., coming from on-track tests performed in Velim (Czech Republic) with the coach UIC-Z1 (see Fig. 4 and 5). The considered vehicle is equipped with a fully-working Wheel Slide Protection (WSP) system.[41][43]
The experimental tests have been carried out on a straight railway track. The wheel profile is the ORE S1002 (with a wheelset width d_w equal to 1.5m and a wheel radius r equal to 0.445m) while the rail profile is the UIC60 (with a gauge d_r equal to 1.435m and a laying angle equal to $1/20$rad). In Tab. 4 the main wheel, rail and contact parameters are reported. [35][34][3])
The value of the kinetic friction coefficient under degraded adhesion conditions μ_{cd}

Table 4 Main wheel, rail and contact parameters

Parameter	Units	Value
Young modulus	[Pa]	$2.1 * 10^{11}$
Shear modulus	[Pa]	$8.0 * 10^{10}$
Poisson coefficient	[Ns/m]	0.3
Contact damping constant	-	$1.0 * 10^{5}$
Polach reduction factor k_{ad}	-	0.3
Polach reduction factor k_{sd}	-	0.1
Polach reduction factor k_{ar}	-	1.0
Polach reduction factor k_{sr}	-	0.4
Kinetic friction coeffcient μ_{cd}	-	0.06
Kinetic friction coeffcient μ_{cr}	-	0.28
Friction ratio A_d	-	0.40
Friction ratio A_r	-	0.40
Friction decrease rate γ_d	[s/m]	0.20
Friction decrease rate γ_r	[s/m]	0.60

depends on the test performed on the track; the degraded adhesion conditions are usually reproduced using a watery solution containing surface-active agents, e.g. a solution sprinkled by a specially provided nozzle directly on the wheel-rail interface on the first wheelset in the running direction. The surface-active agent concentration in the solution varies according to the type of test and the desired friction level. The value of the kinetic friction coefficient under full adhesion recovery μ_{cr} corresponds to the classical kinetic friction coefficient under dry conditions.
During the experimental campaign six different braking tests have been performed. The six tests have been split into two groups (A and B): the first group has been used to tune the degraded adhesion model (in particular the unknow parameter τ, see chapter 3.2.3, Eq. (9)) while the second one to properly validate the tuned model. The initial vehicle velocities correspoding to the considered tests are reported in Tab. 5.
For each test the following physical quantities have been experimentally measured (with a sample time Δt_s equal to 0.01s):

- the longitudinal vehicle velocity v_v^{sp}. For the sake of simplicity all the longitudinal wheel velocities v_{wj}^{sp} (j represents the $j-th$ wheel) are considered equal to v_v^{sp}. The acceleration of the vehicle a_v^{sp} and of the wheels a_{wj}^{sp} can be obtained by derivation and by properly filtering the numerical noise.
- the rotation velocities of all the wheels ω_{wj}^{sp}.

Table 5 Test initial velocities

Initial velocities	Units	Value
Group A, I test	[m/s]	42.3
Group A, II test	[m/s]	40.4
Group A, III test	[m/s]	40.8
Group B, I test	[m/s]	40.8
Group B, II test	[m/s]	41.1
Group B, III test	[m/s]	41.8

- the vertical loads N_{wj}^{sp} on the wheels. The vertical contact forces N_{cj}^{sp} can be approximately evaluated starting from N_{wj}^{sp} by taking into account the weight of the wheels. Also in this case the angular accelerations $\dot{\omega}_{wj}^{sp}$ can be calculated by derivation and by properly filtering.
- the traction or braking torques C_{wj}^{sp} applied to the wheels.

By way of example in Fig. 13 the wheel translational and rotational velocities v_{w1}^{sp} and $r\omega_{w1}^{sp}$ are reported for the I test of the group A; both the WSP intervention and the adhesion recovery in the second part of the braking maneuver are clearly visible.
On the base of the measured data, the experimental outputs of the degraded adhe-

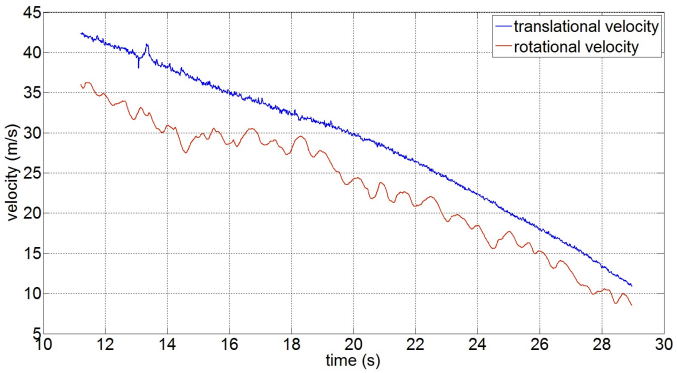

Fig. 13 Wheel translational and rotational velocities v_{w1}^{sp} and $r\omega_{w1}^{sp}$ for the I test of the group A

sion model, e.g. the adhesion coefficient f_j^{sp}, the tangential contact force T_{cj}^{sp} and the transition function λ_j^{sp} have now to be computed for all the tests. These experimental quantities are foundamental for the validation both of the degraded adhesion model (chapter 5) and of the whole multibody model (chapter 6). To reach this goal and to effectively exploit the measured data, in this phase the wheelset is supposed to be placed in its centered position; in this way the position of the single contact point P_c can be supposed to be known and nearly constant and the surface curvatures in the contact points, the semi-axes of the contact patch a, b and the contact shear stiffness C can be easily calculated [26]. Moreover the following simplified expressions for

the sliding s_j^{sp}, for the creepage e_j^{sp} and for C hold:

$$s_j^{sp} = v_{wj}^{sp} - r\omega_{wj}^{sp} \; e_j^{sp} = \frac{s_j^{sp}}{v_{wj}^{sp}} \qquad C = \frac{3Gc_{11}}{8a}. \tag{18}$$

Starting from s_j^{sp} and e_j^{sp}, T_{cj}^{sp} can be estimated through the rotational equilibrium of the wheel with respect to the origin G_w:

$$J_w \dot{\omega}_{wj}^{sp} = C_{wj}^{sp} - rT_{cj}^{sp} \tag{19}$$

in which $J_w = 160\text{kgm}^2$ is the wheel inertia. Subsequently Eq. (7) permits to calculate f_j^{sp} and the specific dissipation energy W_{spj}^{sp} while f_{dj}^{sp}, f_{rj}^{sp} can be computed directly through Eq. (10). Finally, from the knowledge of W_{spj}^{sp} and f_j^{sp}, f_{dj}^{sp}, f_{rj}^{sp}, the trend of the experimental transition function $\lambda_j^{sp}(W_{spj}^{sp})$ can be determined by means of Eq. (8). For instance in Fig. 14 the adhesion coefficient f_1^{sp} and its limit values f_{d1}^{sp}, f_{r1}^{sp} under degraded adhesion and adhesion recovery are illustrated always for the I test of the group A (the adhesion recovery in the second part of the braking maneuver is clear). Fig. 15 shows the experimental trend of the transition function λ_1^{sp}.

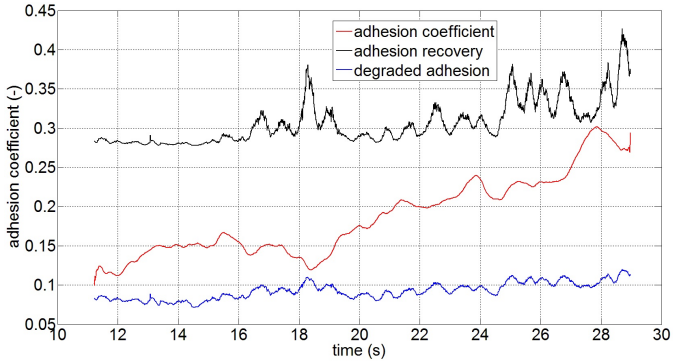

Fig. 14 Adhesion coefficient f_1^{sp} and its limit values f_{d1}^{sp}, f_{r1}^{sp} for the I test of the group A

5 Tuning and Validation of the Degraded Adhesion Model

In this chapter the tuning and the validation of the degraded adhesion model will be described. Both the tuning and the validation will be performed without considering the complete vehicle dynamics that, on the contrary, will be taken into account in the chapter 6.

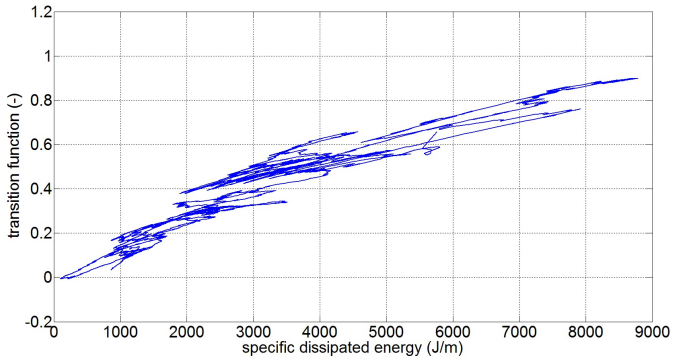

Fig. 15 Experimental transition function $\lambda_1^{sp}(W_{sp1}^{sp})$ for the I test of the group A

5.1 Model Tuning

During this phase of the research activity, the degraded adhesion model has been tuned on the base of the three experimental braking tests of the group A. In particular the attention focused on the transition function $\lambda(W_{sp})$ and on the τ parameter. Starting from the experimental transition functions $\lambda_j^{sp}(W_{spj}^{sp})$ corresponding to the three tests of the group A, the parameter τ within $\lambda(W_{sp})$ has been tuned through a Non-linear Least Square Optimization (NLSO) by minimizing the following error function: [33][28][1]

$$g(\tau) = \sum_{i=1}^{N_t} \sum_{j=1}^{N_w} \left[\lambda_j^{sp}(W_j^{sp}(t_i)) - \lambda(W_j^{sp}(t_i)) \right]^2 \tag{20}$$

where N_w is the wheel number and N_t is the measured sample number. In this case the optimization process provided the optimum value $\tau = 1.9 * 10^{-4}\mathrm{m/J}$. For instance the comparisons between the optimized analytical transition function $\lambda(W_{sp})$ and the experimental transition function $\lambda_1^{sp}(W_{sp1}^{sp})$ are shown for the three tests of the group A in Fig. 16, 17 and 18.

Subsequently, always for the tests of the group A, the adhesion coefficient f_j has been calculated according to chapter 3.2.3 by means of Eq. (15) starting from the knowledge of the experimental inputs v_{wj}^{sp}, ω_{wj}^{sp} and N_{cj}^{sp}; as in chapter 4, the simplified relations of Eq. (18) have been employed. In this circumstance the optimized analytical transition function $\lambda(W_{sp})$ has been used. The behaviour of the calculated adhesion coefficient f_j has been compared with the experimental one f_j^{sp} (see chapter 4). By way of example, in Fig. 19, 20, 21 the time histories of f_1 and f_1^{sp} are reported for all the tests of the group A.

The results of the tuning process hightlight the good capability of the simple analytical transition function, $\lambda(W_{sp})$ in reproducing the experimental trend of $\lambda_j^{sp}(W_{spj}^{sp})$ for all the tests of the group A. The good behaviour of the analytical transition function dispite its simplicity (only one unknown parameter is involved), allows also a good matching of the experimental data in terms of the adhesion coefficient (see the trend of f_j and f_j^{sp} and the adhesion recovery in the second part of the braking maneuver).

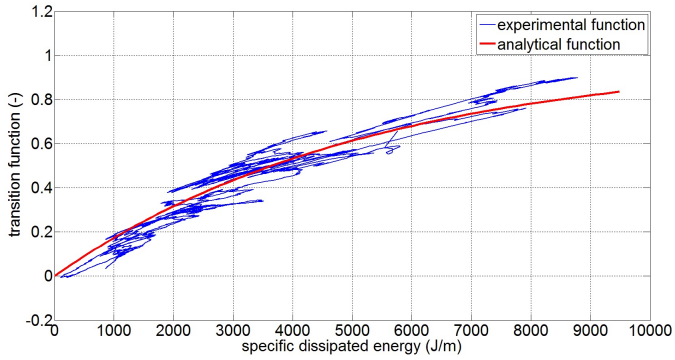

Fig. 16 Comparison between $\lambda(W_{sp})$ and $\lambda_1^{sp}(W_{sp1}^{sp})$ for the I test of the group A

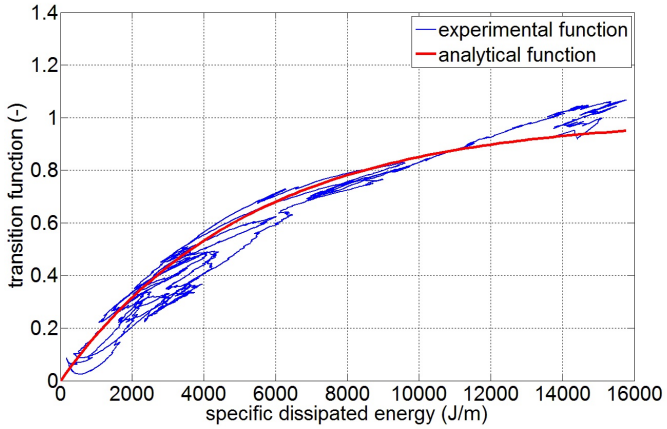

Fig. 17 Comparison between $\lambda(W_{sp})$ and $\lambda_1^{sp}(W_{sp1}^{sp})$ for the II test of the group A

5.2 Model Validation

The real validation of the degraded adhesion model has been carried out by means of the three experimental braking tests of the group B. Also in this case the attention focused, first of all, on the analytical transition function $\lambda(W_{sp})$ (the same tuned in paragraph 5.1 with $\tau = 1.9 * 10^{-4}$m/J) and on its capability in matching the behaviour of the experimental transition functions $\lambda_j^{sp}(W_{spj}^{sp})$. The comparison between $\lambda(W_{sp})$ and $\lambda_1^{sp}(W_{sp1}^{sp})$ is illustred in Fig. 22, 23, 24 for the tests of the group B.

Similarly to paragraph 5.1 the adhesion coefficient f_j has been calculated for the tests of the group B (see chapter 3.2.3 and Eq. (15)) starting from the knowledge of the experimental inputs v_{wj}^{sp}, ω_{wj}^{sp} and N_{cj}^{sp} (the simplified relations of Eq. (18) in chapter 4 have been used). Obviously, the same analytical transition function $\lambda(W_{sp})$ optimized in paragraph 5.1 has been employed. The behaviour of the calculated adhesion coefficient f_j and the experimental one f_j^{sp} (see chapter 4) have been compared again. For instance in Fig. 25, 26, 27 the time histories of f_1 and f_1^{sp} are reported for

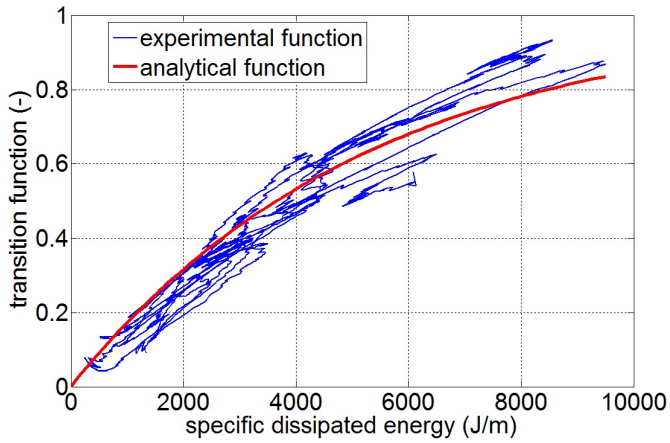

Fig. 18 Comparison between $\lambda(W_{sp})$ and $\lambda_1^{sp}(W_{sp1}^{sp})$ for the III test of the group A

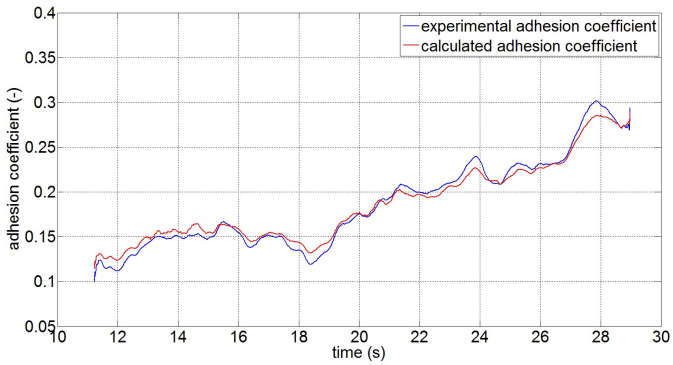

Fig. 19 Comparison between f_1 and f_1^{sp} for the I test of the group A

all the tests of the group B.

The results of the model validation are encouraging and highlight the good matching between the analytical transition function $\lambda(W_{sp})$ (tuned in paragraph 5.1 on the base of the tests of the group A) and the new experimental data $\lambda_j^{sp}(W_{spj}^{sp})$ corresponding to the tests of the group B. At the same time, also for the group B, there is a good correspondence between the time histories of the calculated adhesion coefficient f_j and those of the experimantal one f_j^{sp} (see the adhesion recovery in the second part of the braking maneuver). The satisfying results obtained for the validation group B confirm the capability of the simple analytical transition function $\lambda(W_{sp})$ in approximating the complex and highly non-linear behaviour of the degraded adhesion.

Moreover the new degraded adhesion model present two important advantages. Firstly, it only introduces one additional parameter (e.g. the τ rate), very easy to be experimentally tuned, without requiring the knowledge of further unknown physical properties of the contaminant. Secondly, the model guarantees a very low computational load, making possible the online implementation of the procedure within more gen-

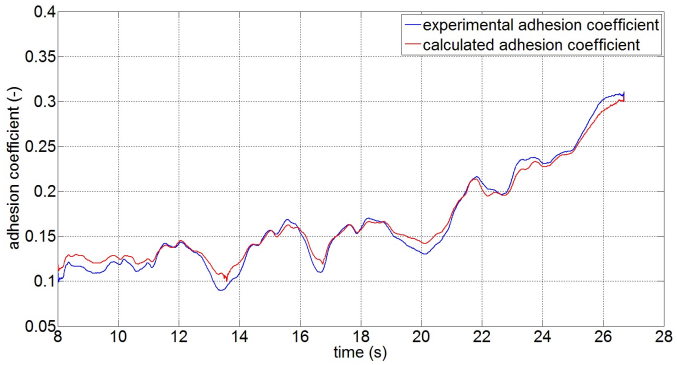

Fig. 20 Comparison between f_1 and f_1^{sp} for the II test of the group A

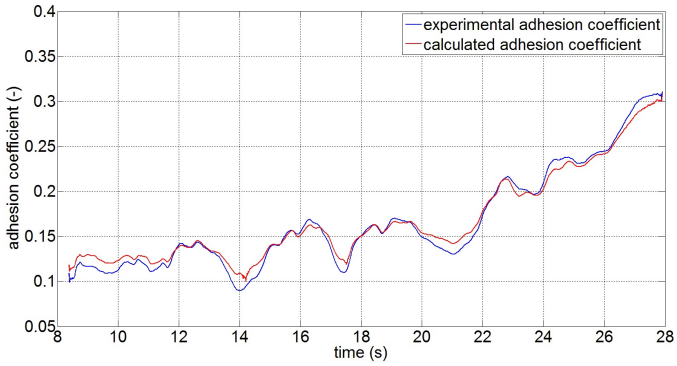

Fig. 21 Comparison between f_1 and f_1^{sp} for the III test of the group A

eral multibody models built in dedicated environments. [1][2]

6 The Validation of the Whole Multibody Model

In this chapter the behaviour of the complete multibody model described in chapter 3 will be analyzed. The vehicle dynamic analysis is focused on the translation and rotational wheel velocities v_{wj}, $r\omega_{wj}$ corresponding to the tests of the tuning group A and the validation group B; more precisely, in this case v_{wj} is the longitudinal component of $\underline{v}_{wj}$, ω_{wj} is the component of $\underline{\omega}_{wj}$ along the wheel rotation axis and, for the sake of simplicity, r is always the nominal wheel radius. These variables have been chosen bacause they are the most important physical quantities in a braking maneuver under degraded adhesion conditions.

In the simulations described in the chapter, the inputs are just the braking torques applied to the wheels C_{wj}^{sp} (experimentally measured); besides, of course, the geometrical and physical characteristics of the track and the vehicle, and the initial conditions of the bodies (in terms of position and speed), are known.

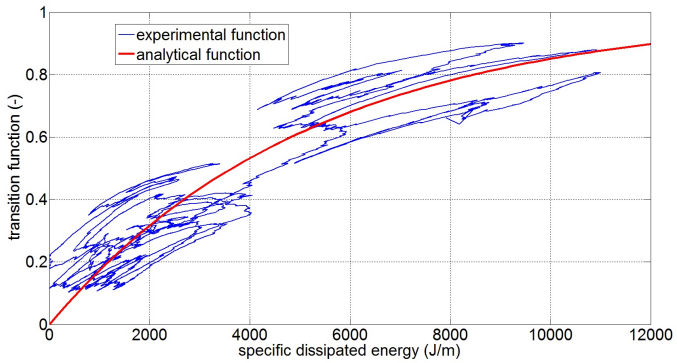

Fig. 22 Comparison between $\lambda(W_{sp})$ and $\lambda_1^{sp}(W_{sp1}^{sp})$ for the I test of the group B

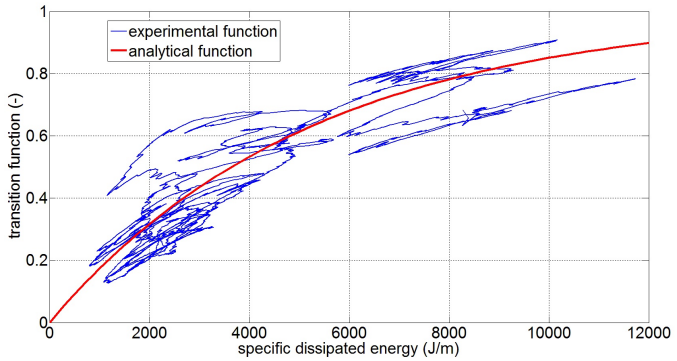

Fig. 23 Comparison between $\lambda(W_{sp})$ and $\lambda_1^{sp}(W_{sp1}^{sp})$ for the II test of the group B

Consequently, the translational and rotational wheel velocities v_{wj}, $r\omega_{wj}$ are in this case fully simulated and, subsequently, compared to the related experimental quantities v_{wj}^{sp}, $r\omega_{wj}^{sp}$ (see chapter 4).

By way of example the time histories of the translational velocities v_{w1}, v_{w1}^{sp} and the rotational velocities $r\omega_{w1}$, $r\omega_{w1}^{sp}$ are reported in Fig. 28, 29, 30 and Fig. 31, 32, 33 for all the three tests of the groups A and B.

Additionally the maximum velocity errors E_j for all the performed tests are considered as well (see the Tab. 6 for E_1):

$$E_j = \max_{t\in[T_I,T_F]} \left| v_{wj}^{sp} - v_{wj} \right|. \tag{21}$$

The results of the analysis show a good agreement in terms of translational velocities v_{wj}, v_{wj}^{sp}, especially in the second part of the braking maneuver where the adhesion recovery occurs. Concerning the rotational velocities $r\omega_{wj}$, $r\omega_{wj}^{sp}$ (and thus the angular velocities) the matching is satisfying. However these physical quantities cannot be locally compared to each other because of the complexity and the chaoticity of the system due, for instance, to the presence of discontinuous and non-linear thresh-

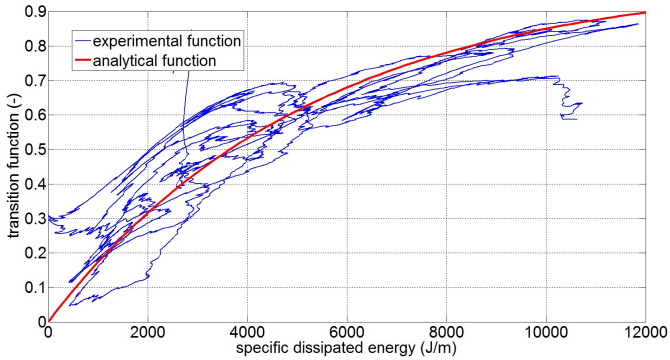

Fig. 24 Comparison between $\lambda(W_{sp})$ and $\lambda_1^{sp}(W_{sp1}^{sp})$ for the III test of the group B

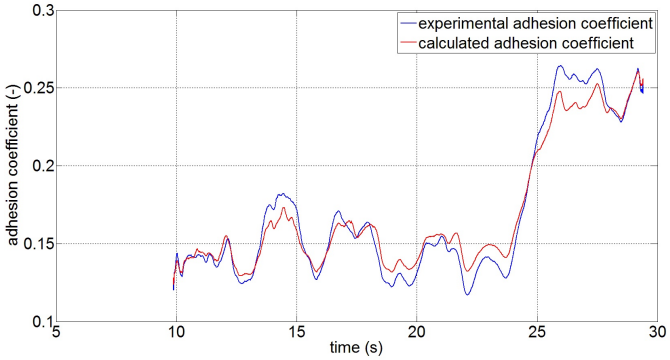

Fig. 25 Comparison between f_1 and f_1^{sp} for the I test of the group B

Table 6 Maximum velocity errors E_1, sliding means $\bar{s}_1$, $\bar{s}_1^{sp}$ and sliding standard deviations Δ_1, Δ_1^{sp}

Parameter	Units	A1	A2	A3	B1	B2	B3
E_1	[m/s]	2.05	0.90	1.84	1.51	0.91	1.68
$\bar{s}_1^{sp}$	[m/s]	5.00	5.25	4.23	5.49	5.41	5.83
$\bar{s}_1$	[m/s]	5.61	4.96	4.61	5.14	5.30	5.73
Δ_1^{sp}	[m/s]	1.72	2.19	1.59	1.75	1.77	1.78
Δ_1	[m/s]	1.49	1.79	1.59	1.58	1.45	1.84

old elements like the WSP. To better evaluate the behaviour of $r\omega_{wj}$ and $r\omega_{wj}^{sp}$ from a global point of view, it is usefull to introduce the statistical means $\bar{s}_j$, $\bar{s}_j^{sp}$ and standard deviations Δ_j, Δ_j^{sp} of the calculated slidings s_j and of the experimantal ones s_j^{sp}:

$$\begin{aligned} s_j &= v_{wj} - r\omega_{wj} \\ s_j^{sp} &= v_{wj}^{sp} - r\omega_{wj}^{sp}; \end{aligned} \tag{22}$$

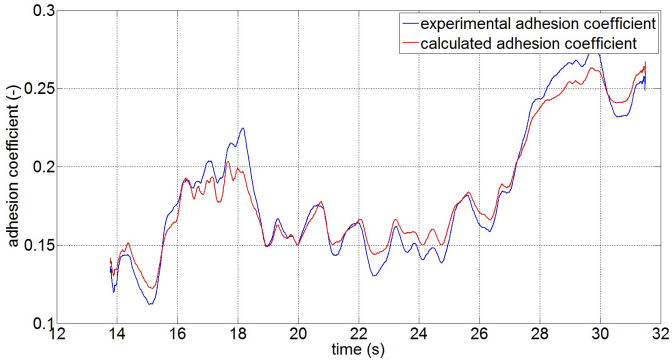

Fig. 26 Comparison between f_1 and f_1^{sp} for the II test of the group B

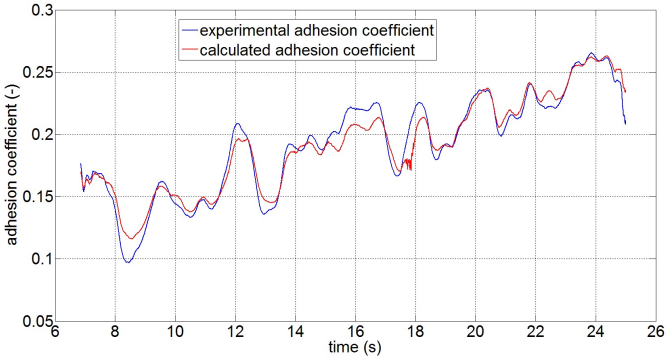

Fig. 27 Comparison between f_1 and f_1^{sp} for the III test of the group B

the statistical indices are then evaluated as follows:

$$\begin{aligned} \bar{s}_j &= \frac{1}{T_F - T_I} \int_{T_I}^{T_F} s_j dt \\ \bar{s}_j^{sp} &= \frac{1}{T_F - T_I} \int_{T_I}^{T_F} s_j^{sp} dt \\ \Delta_j &= \sqrt{\frac{1}{T_F - T_I} \int_{T_I}^{T_F} (s_j - \bar{s}_j)^2 dt} \\ \Delta_j^{sp} &= \sqrt{\frac{1}{T_F - T_I} \int_{T_I}^{T_F} (s_j^{sp} - \bar{s}_j^{sp})^2 dt} \end{aligned} \tag{23}$$

where T_I and T_F are initial and final times of the simulation respectively. For instance the means $\bar{s}_1$, $\bar{s}_1^{sp}$ and the standard deviations Δ_1, Δ_1^{sp} of the slidings s_1, s_j^{sp} are summarized in Tab. 6 for all the three tests of the groups A and B; they confirm the good matching also in terms of slidings and rotational velocities.
In conclusion, the numerical simulations of the vehicle dynamics during the braking maneuver highlight again the capability of the developed model in approximating the complex and highly non-linear behaviour of the degraded adhesion. The result

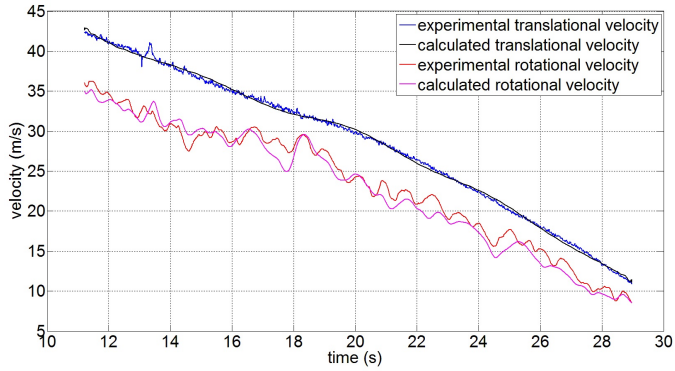

Fig. 28 Translational velocities v_{w1}, v_{w1}^{sp} and rotational velocities $r\omega_{w1}$, $r\omega_{w1}^{sp}$ of the I test fo the group A

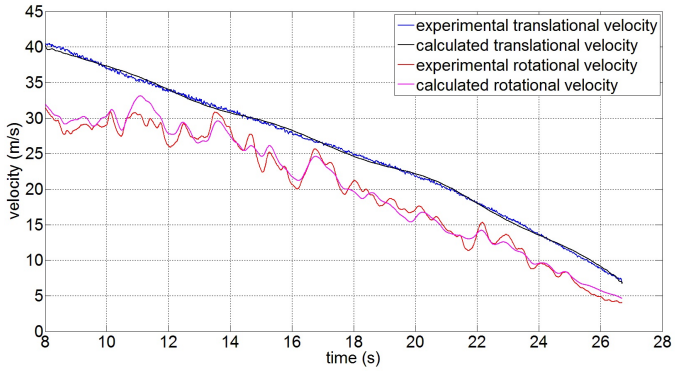

Fig. 29 Translational velocities v_{w1}, v_{w1}^{sp} and rotational velocities $r\omega_{w1}$, $r\omega_{w1}^{sp}$ of the II test fo the group A

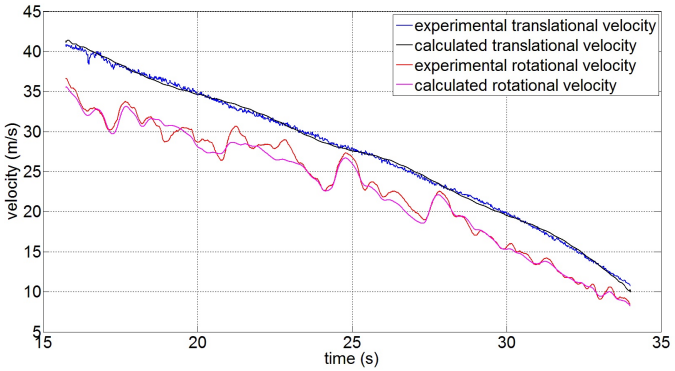

Fig. 30 Translational velocities v_{w1}, v_{w1}^{sp} and rotational velocities $r\omega_{w1}$, $r\omega_{w1}^{sp}$ of the III test fo the group A

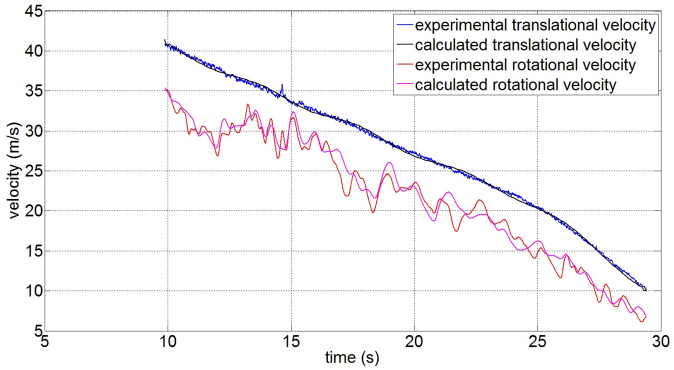

Fig. 31 Translational velocities v_{w1}, v_{w1}^{sp} and rotational velocities $r\omega_{w1}$, $r\omega_{w1}^{sp}$ of the I test fo the group B

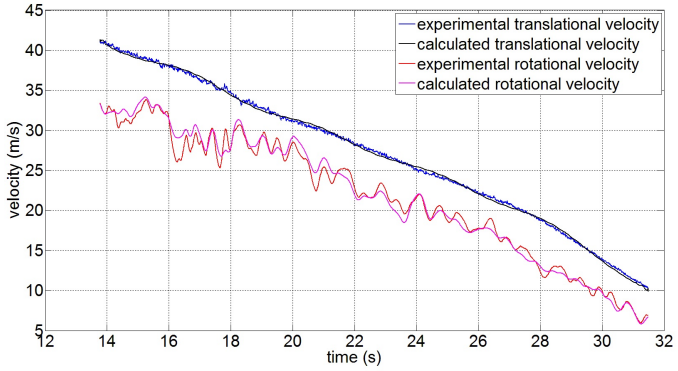

Fig. 32 Translational velocities v_{w1}, v_{w1}^{sp} and rotational velocities $r\omega_{w1}$, $r\omega_{w1}^{sp}$ of the II test fo the group B

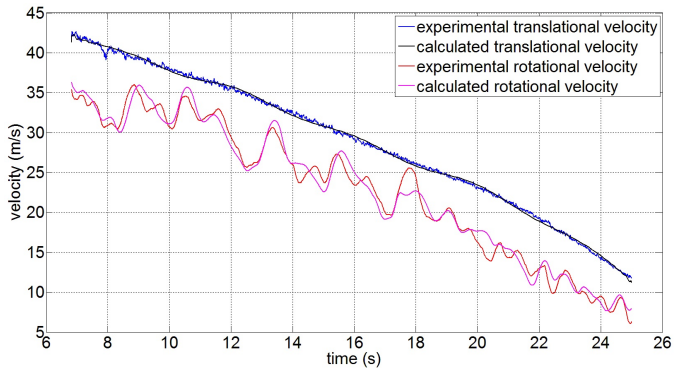

Fig. 33 Translational velocities v_{w1}, v_{w1}^{sp} and rotational velocities $r\omega_{w1}$, $r\omega_{w1}^{sp}$ of the III test fo the group B

is encouraging especially considering the simplicity of the whole model (only one unknown parameter is involved) and the computational times are very low.

7 Computational Times

As previously said inside the paper, the wheel-rail contact model comprising the new degraded adhesion model is suitable for multibody applications, very important in the study of the railway vehicle dynamics. In particular high computational performances are required so that the contact model could be directly implemented online within more general multibody models developed in dedicated environments (in this case Matlab-Simulink). [1][2]
The data corresponding to the CPU employed in the numerical simulations (see chapter 6) and the main integration parameters of the ordinary differential equations (ODE) solver are reported in Tab. 7. [40][1]
To verify the computational efficiency of the new degraded adhesion model, the simulation times concerning the whole railway vehicle model (3D multibody model of the vehicle and 3D wheel rail contact model) have been measured. The computation times reported in Tab. 8 are referred to the I test of the group A and are divided into the computation times related to the 3D multibody vehicle model and the ones related to the 3D wheel-rail contact model. More particularly, four different contact models (always implemented directly online within the multibody model of the vehicle) have been considered. All the contact models share the same contact point detection algorithm [31][9][20] and the solution of the normal problem [6][10][26] while, as regards the tangential contact problem, the following options have been taken into account: the global Kalker theory saturated through the Johnson-Vermeulen formula [26][25], the Kalker FASTSIM algorithm [26][27], the Polach model [35][34] and the new degraded adhesion model.
As the results summarized in Tab. 8 show, the numerical efficiency of the new

Table 7 CPU data and integration parameters

Parameter	Units	Parameter
CPU	-	INTEL Xeon E5430 2.66GHz, 8GB RAM
Integrator type	-	ODE5
Algorithm	-	Dormand-Prince
Order	-	5
Step type	-	Fixed
Stepsize Δt	[s]	10^{-4}

Table 8 Computation times of the different wheel-rail contact models

Contact Model Type	3D Multibody Vehicle Model	3D Contact Model	Whole Model
Global Kalker theory	232s	118s	350s
Kalker FASTSIM algorithm	235s	213s	449s
Polach model	232s	128s	360s
New degraded adhesion model	232s	130s	362s

degraded adhesion model is substantially the same of the other wheel-rail contact models that do not consider degraded adhesion conditions. The achievement of this goal has been possible thanks to the simplicity of the new procedure and allows an easy and efficient online implementability of the adhesion model within more generic multibody models.

8 Conclusions and Further Developments

In this work the authors presented a model aimed to obtain a better accuracy in describing degraded adhesion conditions at the wheel-rail interface in railway vehicle dynamics. The new approach is suitable for multibody applications (e.g. in Matlab-Simulink and Simpack environments), very important in the considered research area, and assures high computational performances making possible the direct online implementation of the degraded adhesion model within more general vehicle multibody models.
The new model is based on the main phenomena characterising the degraded adhesion, such as the energy dissipation at the contact interface, the consequent cleaning effect and the resulting adhesion recovery due to the removal of external unknown contaminants. Since most of the physical characteristics of the contaminants are totally unknown in practice, the new approach minimizes the number of hardly measurable physical quantities required by the model.
The adhesion model has been validated thanks to experimental data provided by Trenitalia S. p. A. coming from on-track tests performed in Velim (Czech Republic) with the railway vehicle UIC-Z1. The tests have been carried out on a straight railway track under degraded adhesion conditions with a vehicle equipped with a Wheel Slide Protection (WSP) system.
Many important developments are scheduled for the future. Firstly further experimental tests will be carried out by Trenitalia concerning both braking and traction phases. The new experimental data will allow a better tuning of the geometrical and physical parameters of the model.
Secondly some improvements of the model will be taken into account. Particularly new theoretical and experimental relations among the adhesion coefficient f, the specific dissipated energy W_{sp} and the limit adhesion levels f_d, f_r (degraded adhesion and adhesion recovery) will be studied.
Finally the new degraded adhesion model will be applied to the study of railway vehicle dynamics and wheel-rail contact on generic railway tracks and networks both in terms of accuracy (comparing it with different contact and adhesion models that do not take into account the adhesion recovery) and computational efficiency. To this end, different kinds of wheel and track irregularities will be also included in the proposed scenarios. This way some important topics such as the profile evolution due to wear, the profile optimization and the development of innovative railway bogies will be further and more deeply investigated.

9 Acknowledgements

The authors would like to thank the Trenitalia archives for supplying the experimental data relative to the braking tests under degraded adhesion conditions.

References

1. www.mathworks.com. Official Site of Mathworks, Natick, MA, USA (2012)
2. www.simpack.com. Official Site of Simpack GmbH, Gilching, Germany (2012)
3. Railway applications, braking, wheel slide protection. UNI EN 15595 (Milano, Maggio 2009)
4. Allotta, B., Conti, R., Malvezzi, M., Meli, E., Pugi, L., Ridolfi, A.: Numerical simulation of a hil full scale roller-rig model to reproduce degraded adhesion conditions in railway applications. In: European Congress on Computational Methods in Applied Sciences and Engineering (ECCOMAS 2012). Austria (2012)
5. Allotta, B., Malvezzi, M., Pugi, L., Ridolfi, A., Rindi, A., Vettori, G.: Evaluation of odometry algorithm performances using a railway vehicle dynamic model. Vehicle System Dynamics **50**(5), 699–724 (2012)
6. Antoine, J., Visa, C., Sauvey, C., Abba, G.: Approximate analytical model for hertzian elliptical contact problems. Journal of Tribology **128**, 660–664 (2006)
7. Arias-Cuevas, O., Li, Z., Lewis, R.: A laboratory investigation on the influence of the particle size and slip during sanding on the adhesion and wear in the wheelrail contact. Wear **271**, 14–24 (2011)
8. Arias-Cuevas, O., Li, Z., Lewis, R., Gallardo-Hernandez, E.: Rollingsliding laboratory tests of friction modifiers in dry and wet wheelrail contacts. Wear **268**, 543–551 (2010)
9. Auciello, J., Meli, E., Falomi, S., Malvezzi, M.: Dynamic simulation of railway vehicles: wheel/rail contact analysis. Vehicle System Dynamics **47**, 867–899 (2009)
10. Ayasse, J., Chollet, H.: Determination of the wheel rail contact patch in semi-hertzian conditions. Vehicle System Dynamics **43**, 161–172 (2005)
11. Blau, P.J.: Embedding wear models into friction models. Tribology Letters **34**, 75–79 (2009)
12. Boiteux, M.: Le probleme de l'adherence en freinage. Revue generale des chemins de fer pp. 59–72 (1986)
13. Cheli, F., Pennestr, E.: Cinematica e dinamica dei sistemi multibody. CEA, Milano, Italia (2006)
14. Chen, H., Ban, T., Ishida, M., Nakahara, T.: Experimental investigation of influential factors on adhesion between wheel and rail under wet conditions. Wear **265**, 1504–1511 (2008)
15. Conti B. Meli, E., Pugi, L., Malvezzi, M., Bartolini, F., Allotta B. Rindi, A., Toni, P.: A numerical model of a hil scaled roller rig for simulation of wheelrail degraded adhesion condition. Vehicle System Dynamics **50**(5), 775–804 (2012)
16. Descartes, S., Desrayaud, C., Niccolini, E., Berthier, Y.: Presence and role of the third body in a wheelrail contact. Wear **258**, 1081–1090 (2005)
17. Dukkipati, R., Amyot, J.: Computer Aided Simulation in Railway Dynamics. Dekker, New York, USA (1988)
18. Eadie, D., Kalousek, J., Chiddick, K.: The role of high positive friction (hpf) modifier in the control of short pitch corrugations and related phenomena. Wear **253**, 185–192 (2002)
19. Esveld, C.: Modern Railway Track. Delft University of Technology, Delft, Netherlands (2001)
20. Falomi, S., Malvezzi, M., Meli, E.: Multibody modeling of railway vehicles: innovative algorithms for the detection of wheel-rail contact points. Wear **271**(1-2), 453–461 (2011)
21. Gallardo-Hernandez, E., Lewis, R.: Twin disc assessment of wheel/rail adhesion. Wear **265**, 1309–1316 (2008)
22. Ignesti, M., Malvezzi, M., Marini, L., Meli, E., Rindi, A.: Development of a wear model for the prediction of wheel and rail profile evolution in railway systems. Wear **284-285**, 1–17 (2012)
23. Iwnicki, S.: Simulation of wheel - rail contact forces. Fatigue and Fracture of Engineering Materials and Structures **26**, 887–900 (2003)
24. Iwnicki, S.: Handbook of Railway Vehicle Dynamics. Taylor and Francis (2006)
25. Johnson, K.: Contact Mechanics. Cambrige University Press, Cambridge, UK (1985)
26. Kalker, J.: Three-Dimensional Elastic Bodies in Rolling Contact. Kluwer Academic Publishers, Norwell, MA (1990)

27. Kalker, J.J.: A fast algorithm for the simplified theory of rolling contact. Vehicle System Dynamics **11**, 1–13 (1982)
28. Kelley, C.: Iterative methods for linear and nonlinear equations. SIAM, Philadelphia PA, USA (1995)
29. Magheri, S., Malvezzi, M., Meli, E., Rindi, A.: An innovative wheel-rail contact model for multibody applications. Wear **271**(1-2), 462–471 (2011)
30. Malvezzi, M., Pugi, L., Ridolfi, A., Cangioli, F., Rindi, A.: Three dimensional modelling of wheel-rail degraded adhesion conditions. In: Proceedings of IAVSD 2011. Manchester (2011)
31. Meli, E., Falomi, S., Malvezzi, M., Rindi, A.: Determination of wheel - rail contact points with semi-analytic methods. Multibody System Dynamics **20**(4), 327–358 (2008)
32. Niccolini, E., Berthier, Y.: Wheelrail adhesion: laboratory study of natural third body role on locomotives wheels and rails. Wear **258**, 1172–1178 (2005)
33. Nocedal, J., Wright, S.: Numerical optimization. Springer Series in Operation Research, Berlin, Germany (1999)
34. Polach, O.: A fast wheelrail forces calculation computer code. Vehicle System Dynamics **33**, 728–739 (1999)
35. Polach, O.: Creep forces in simulations of traction vehicles running on adhesion limit. Wear **258**, 992–1000 (2005)
36. Pombo, J., Ambrosio, J.: Application of a wheelrail contact model to railway dynamics in small radius curved tracks. Multibody System Dynamics **19**, 91–114 (2008)
37. Pombo, J., Silva, A.: A new wheelrail contact model for railway dynamics. Vehicle System Dynamics **45**, 165–189 (2007)
38. Shabana, A., Tobaa, M., Sugiyama, H., Zaazaa, K.: On the computer formulations of the wheel/rail contact problem. Nonlinear Dynamics **40**, 169–193 (2005)
39. Shabana, A., Zaza, K., J.E., E., J.R., S.: Development of elastic force model for wheel/rail contact problems. Journal of Sound and Vibration **269**, 295–325 (2004)
40. Shampine, L., Reichelt, M.: The matlab ode suite. SIAM Journal of Scientific Computation **18**, 1–22 (1997)
41. TrenitaliaSpA: UIC-Z1 coach. Internal report of Trenitalia, Rome, Italy (2000)
42. TrenitaliaSpA: On-track braking tests. Internal report of Trenitalia, Rome, Italy (2005)
43. TrenitaliaSpA: WSP systems. Internal report of Trenitalia, Rome, Italy (2006)
44. Voltr, P., Lata, M., Cerny, O.: Measuring of wheel-rail adhesion characteristics at a test stand. In: XVIII Internation Conference on Engineering Mechanics. Czech Republic (2012)
45. Wang, W., Zhang, H., Wang, H., Liu, Q., Zhu, M.: Study on the adhesion behavior of wheel/rail under oil, water and sanding conditions. Wear **271**, 2693–2698 (2011)
46. Zhang, W., Chen, J., Wu, X., Jin, X.: Wheel/rail adhesion and analysis by using full scale roller rig. Wear **253**, 82–88 (2002)